

# Dynamic mmWave Channel Emulation in a Cost-Effective MPAC with Dominant-Cluster Concept

Xuesong Cai, *Member, IEEE*, Yang Miao, Jinxing Li  
Fredrik Tufvesson, *Fellow, IEEE*, Gert Frølund Pedersen, Wei Fan, *Senior Member, IEEE*

**Abstract**—Millimeter-Wave (mmWave) massive multiple-input multiple-output (MIMO) has been considered as a key enabler for the fifth-generation (5G) communications. It is essential to design and test mmWave 5G devices under various realistic scenarios, since the radio propagation channels pose intrinsic limitations on the performance. This requires emulating a realistic dynamic mmWave channels in a reproducible manner in laboratories, which is the goal of this paper. In this contribution, we firstly illustrate the dominant-cluster(s) concept, where the non-dominant clusters in the mmWave channels are pruned, for mmWave 5G devices applying massive MIMO beamforming. This demonstrates the importance and necessity to accurately emulate the mmWave channels at a cluster level rather than the composite-channel level. Thus, an over-the-air (OTA) emulation strategy for dynamic mmWave channels is proposed based on the concept of dominant-cluster(s) in a sectored multiprobe anechoic chamber (SMPAC). The key design parameters including the probe number and the angular spacing of probes are investigated through comprehensive simulations. A cost-effective switch-circuit is also designed for this purpose and validated in the simulation. Furthermore, a dynamic mmWave channel measured in an indoor scenario at 28-30 GHz is presented, where the proposed emulation strategy is also validated by reproducing the measured reality.

**Index terms**— Millimeter-wave, massive MIMO, beamforming, dynamic channels and clusters, over-the-air testing, multiprobe anechoic chamber (MPAC), channel emulation

## I. INTRODUCTION

To meet the needs of immensely increased wireless data consumption driven by a diversity of applications and devices, fifth-generation (5G) networks with even lower latency, higher spectral efficiency, and higher reliability are under deployment. Millimeter-Wave (mmWave) communication with a large amount of available spectrum is one of the key enablers. As the carrier frequencies increase and antenna apertures

decrease significantly, one countermeasure to improve the link margin is massive multiple-input multiple-output (MIMO). A massive MIMO device is expected to establish multiple narrow beams to multiple users and dynamically steer the beams as users move or channel conditions change. In such a way, by combining beamforming and spatial multiplexing, a massive MIMO system can serve unconventionally large number of terminals in the same time-frequency resources [1]–[3]. Nevertheless, the mmWave radio propagation channel poses many challenges such as severe power losses, scattering and blockage from e.g. human body and moving vehicles, etc. [4]–[6]. The uncontrollable dynamic (time-varying) channels not only limit the coverage, but may also cause serious performance degradation, e.g., due to the loss of user tracking. Therefore, it is important to design and evaluate the mmWave devices considering various real-world mmWave channel conditions. However, in-field device testing is always expensive and exposed to unpredictable uncertainties. Moreover, mmWave massive MIMO systems are composed of tens or hundreds of antenna elements as an integrated unit. It is thus neither feasible nor economic to implement conductive testing by connecting each radiating element to radio frequency (RF) cable at mmWave frequencies. Therefore, over-the-air (OTA) testing which refers to test wireless devices in the laboratory environment without cable-connection has become an essential performance validation procedure for mmWave massive MIMO devices. In OTA testing, the actual dynamic channel condition is mimicked in lab as if the devices were put into use in the real-world. It saves time and money and, most importantly, is reproducible hence provides fair assessment of devices.

The OTA testing for mmWave massive MIMO devices must meet the requirements on signal quality, antenna calibration, demodulation (data throughput performance) and radio resource management (RRM) [7]. RRM refers to the initial access to system, the connection reconfiguration, the handover during mobility, the beam refinement and tracking, and it should be based on realistic mmWave channel conditions and dynamic spatial profiles. To meet the above requirements, different OTA testing strategies including reverberation chamber (RC), radiated two stage (RTS) method and multiprobe anechoic chamber (MPAC) have been proposed. In the RC approach, metallic stirrers are used in an enclosed metallic cavity to produce a random field variation. As only uniform

X. Cai and F. Tufvesson are with the Department of Electrical and Information Technology, Lund University, 22100 Lund, Sweden (e-mails: xuesong.cai@eit.lth.se; fredrik.tufvesson@eit.lth.se). The work was started when X. Cai was with the Department of Electronic Systems, Aalborg University, Aalborg 9220, Denmark.

Y. Miao is with the Radio Systems, Faculty of Electrical Engineering Computer Science and Mathematics (EEMCS), University of Twente, the Netherlands (e-mail: y.miao@utwente.nl).

J. Li is with Huawei Technologies, Shanghai Research Institute, Shanghai 201206, China (e-mail: lijinxing3@huawei.com).

G. F. Pedersen and W. Fan are with the Department of Electronic Systems, Aalborg University, Aalborg 9220, Denmark (e-mails: gfp@es.aau.dk; wfa@es.aau.dk).

power angular spectrum (PAS) can be emulated in RC, little control is available over angular distribution and channel depolarization [8], [9]. Since mmWave channels are highly sparse and directive [10], i.e., being dominant by a few propagation paths/clusters, RC is thus less suitable. Nevertheless, reconfigurable RC whose walls support for the reconstruction of controllable 3D PAS is under investigation. For the RTS method [11], [12] which aims to achieve cable connection function without actual RF cables, the transfer function between the probe antennas and the antenna ports of device under test (DUT) are effectively calibrated via implementing an inverse matrix in the channel emulator. It is capable of emulating arbitrary dynamic channel. However, the main drawback is that the antenna systems on the DUT has to remain static (i.e. non-adaptive to the dynamic channel and therefore beam-locked mode enabled). Therefore, it is not a true end-to-end OTA testing method for performance evaluation. In the MPAC approach, the fading emulator synthesizes the fields in the test zone by controlling the excitation and radiation of probes. The MPAC setup can emulate arbitrary PAS and has easier control over the polarization [13]–[17]. To address the bi-directional (both uplink and downlink) and 3D spatial channels for testing mmWave massive MIMO devices, the conventional MPAC configuration has been evolved into the 3D sectored MPAC (SMPAC) configuration as discussed in [7], [18]. The sectored configuration refers to one or a few sector(s) of co-located probes deployed on the partial spherical surface with dual-polarized antennas [7]. The key design parameters include *i*) the measurement range or the distance between DUT and probes, *ii*) the number of probes and *iii*) the amount of mmWave channel emulator resources. These in turn depend on the major clusters of paths in realistic propagation channels and the desired emulation accuracy. While the mmWave probe antennas can be made cheap (e.g., using patch antennas), the associated RF chains connected to the probes including RF cables and up/down-frequency converters<sup>1</sup> as well as the base-band components in a channel emulator are very expensive. Given that the mmWave massive MIMO channel has a highly sparse and directive angular profile, part of the probes maybe inactive during emulation, a probe selection mechanism with a switch-circuit can be used to reduce cost on RF chains while maintaining accuracy. For these advantages, this paper focuses on the SMPAC.

Meanwhile, many measurement campaigns, e.g. [19]–[21], have shown that mmWave channels are sparse and mainly power-limited caused by path loss, blockage, etc. Thus beamforming in mmWave is essential by transmitting coherent signals thus forming a concentrated field to increase signal-to-noise-ratio (SNR) or throughput. This in turn, as shown later in Sect. II-D, filters the channel. Similar demonstration can be found in [22] where the spatial channel at the user equipment (UE) side can be significantly simplified if base station (BS) beamforming operation is applied. In other words, it is not necessary to emulate all the clusters, since some clusters become insignificant with beamforming. Moreover,

<sup>1</sup>Up-frequency converters are required when signals are streamed from the emulator to the DUT, and vice versa.

beams of a BS and UEs should be able to reliably track each other, which means that the dynamic characteristics at a cluster-level is essential to be emulated. Although the existing SMPAC, e.g. in [7], [18], [23], has several advantages over the conventional MPAC, there are still research gaps that need to be addressed considering the above mentioned new mmWave features. Limitations include *i*) All the clusters in the mmWave channel are emulated. The cost of the associated RF resources may be still considerable as a relatively large number of active probes is required if a high emulation accuracy is demanded. *ii*) Since the channel is emulated in a composite manner, cluster-level dynamic characteristics, e.g. of the dominant cluster, may be not well reproduced. However, mmWave massive MIMO communications mainly rely on this dominant cluster. It is essential to reproduce the dominant cluster/clusters with high emulation accuracy for performance evaluation. *iii*) The switch-circuit with full freedom results in high cost and complexity. How to devise a dedicated but low-profiled switching matrix with expected flexibility to support the targeted dynamic channel still needs to be refined.

Overall, the SMPAC setup is promising for OTA testing of mmWave massive MIMO devices. However, the performance of such setup on realizing highly dynamic, sparse and directive mmWave channels is yet to be enhanced with emphasis on cluster-level behavior and lower cost profile. Whether it is possible to emulate a dynamic selection of a limited number of cluster(s) instead of all clusters, to further reduce the cost on RF resources and the complexity of the switch-circuit with dedicated flexibility while maintaining/improving the emulation accuracy and better meeting the testing requirements, is lacking investigation in literature. To fill the above mentioned research gaps, the main contributions of this paper are as follows:

- The beamforming effect of mmWave massive MIMO, i.e. channel simplification, is discussed, which is the basic reasoning for the proposed dominant-cluster(s) concept. This idea has been briefly discussed in the standardization meetings [24], [25], though details were not given. Compared to [24], [25], we propose two different metrics that correspond to beam management and throughput respectively to evaluate the number of cluster(s) that are dominant for OTA emulation.
- Comprehensive simulations have been performed to find proper design parameters. Especially, to our best knowledge, we for the first time distinguish aligned and non-aligned cluster conditions, which is essential for emulating a dynamic cluster evolving in the angular domain. Moreover, a simpler switching matrix is also proposed with interleaved probe panel design.
- Different from most of the other works solely based on simulations, an indoor dynamic mmWave channel measured at 28-30 GHz is presented. The proposed setup is validated using the realistic measurement data.

The rest of the paper is organized as follows. In Sect. II, the system models of mmWave massive MIMO communication, mmWave propagation channels and channel emulation are

elaborated. In Sect. III, we discuss the proposed SMPAC design for dynamic channel emulation via comprehensive simulations. In Sect. IV, the performance of the design is evaluated by exploiting a realistic indoor dynamic mmWave channel. Conclusive remarks are finalized in Sect. V.

## II. SYSTEM MODEL

In this section, we introduce the model of the mmWave massive MIMO communication system, which is useful to help readers understand the theory and practice as well as the resulting limitations upon OTA channel emulation. The signal models of the MIMO channel and OTA channel emulation are also elaborated on. Finally, the effect of beamforming in massive MIMO is illustrated for the dominant-clusters concept.

### A. Wireless Communications Model

In this subsection, we provide a short review for the massive MIMO communication using hybrid array configuration [26]–[28]. As illustrated in Fig. 1, we exemplify the concept with a single-cell downlink wireless communication scenario where one BS and  $U$  UEs are considered. The BS has  $N$  antenna elements and  $N_{\text{RF}}$  RF-chains, and  $N_{\text{S}}$  data streams are transmitted to serve  $U$  users ( $N_{\text{S}} \leq N_{\text{RF}} \leq N$ ). The  $u$ th user has  $M_u$  antenna elements and  $M_{\text{RF},u}$  RF-chains, respectively, and  $M_{\text{S},u}$  data streams are intended for this user ( $M_{\text{S},u} \leq M_{\text{RF},u} \leq M_u$ ). At the BS side, data symbols  $\mathbf{S}(f, t) \in \mathbb{C}^{N_{\text{S}} \times 1}$  to be transmitted at the subcarrier  $f$  and time instant  $t$  are firstly precoded with the baseband digital precoding matrix  $\mathbf{F}_{\text{B}} \in \mathbb{C}^{N_{\text{RF}} \times N_{\text{S}}}$  and then precoded by the RF precoding matrix  $\mathbf{F}_{\text{RF}} \in \mathbb{C}^{N \times N_{\text{RF}}}$  in the RF domain. That is, the complex-equivalent symbol-vector  $\mathbf{X}(f, t) \in \mathbb{C}^{N \times 1}$  sent is formatted as

$$\mathbf{X}(f, t) = \mathbf{F}_{\text{RF}}(f, t)\mathbf{F}_{\text{B}}(f, t)\mathbf{S}(f, t). \quad (1)$$

At the UE side, the received signal  $\mathbf{Y}_u(f, t) \in \mathbb{C}^{M_u \times 1}$  at the  $M_u$  antenna ports of the  $u$ th user is

$$\mathbf{Y}_u(f, t) = \mathbf{H}_u(f, t)\mathbf{X}(f, t) + \mathbf{N}(f, t) \quad (2)$$

where  $\mathbf{N}(f, t)$  represents white Gaussian noise, and  $\mathbf{H}_u(f, t) \in \mathbb{C}^{M_u \times N}$  is the MIMO channel transfer matrix for the  $u$ th user, which is defined later in (4). Similarly,  $\mathbf{Y}_u(f, t)$  is firstly combined in the RF domain by applying the RF combining matrix  $\mathbf{W}_{\text{RF},u} \in \mathbb{C}^{M_u \times M_{\text{B},u}}$  and then combined in the baseband domain with the digital combining matrix  $\mathbf{W}_{\text{B},u} \in \mathbb{C}^{M_{\text{RF},u} \times M_{\text{S},u}}$ . Therefore, the received data symbol vector  $\mathbf{Z}_u(f, t)$  at subcarrier  $f$  after signal-processing is

$$\mathbf{Z}_u = \mathbf{W}_{\text{B},u}^H \mathbf{W}_{\text{RF},u}^H \mathbf{H}_u \mathbf{F}_{\text{RF}} \mathbf{F}_{\text{B}} \mathbf{S} + \mathbf{W}_{\text{B},u}^H \mathbf{W}_{\text{RF},u}^H \mathbf{N} \quad (3)$$

where  $(f, t)$  is omitted for notation conciseness. It is known from (3) that the adaptive  $\mathbf{W}_{\text{RF},u}$  and  $\mathbf{F}_{\text{RF}}$  make it infeasible to reproduce the MIMO channel matrix  $\mathbf{W}_{\text{RF},u}^H \mathbf{H}_u \mathbf{F}_{\text{RF}}$ , e.g. using the RTS method. The proper solution for hybrid massive MIMO should be reproducing  $\mathbf{H}_u$ . Moreover, to reduce the system overhead in estimating and/or feedbacking the instantaneous channel state information, the major approach in practice to enable mmWave massive MIMO is that the

BS and UE perform joint beam-sweeping using predefined codebooks and then choose the best beam for communication, e.g. as specified in the standardization document [29], which means that the dominant cluster/clusters in the channel is/are essential.

### B. MIMO Channel Model

The channel transfer matrix  $\mathbf{H}(f, t)$  in (2) is attributed to both the radio propagation environment and the antenna radiation patterns of BS and UE.<sup>2</sup> It is also time-dependent for dynamic channels as the propagation delays, complex polarimetric gains, angles, Doppler frequencies, etc. of multipath components are evolving. The widely applied geometrical channel model for  $\mathbf{H}(f, t)$  can be formatted as

$$\begin{aligned} \mathbf{H}(f, t) = & \sum_{\ell=1}^{L(t)} \mathbf{G}_{\text{Rx}}(f, -\mathbf{k}_{\ell}^{\text{Rx}}(t)) \mathbf{A}_{\ell}(f, t) \mathbf{G}_{\text{Tx}}^T(f, \mathbf{k}_{\ell}^{\text{Tx}}(t)) \\ & \times \exp\{j2\pi \int_0^t \nu_{\ell}(t') dt'\} \exp\{-j2\pi f \tau_{\ell}(t)\} \end{aligned} \quad (4)$$

with  $\mathbf{A}_{\ell}(f, t) \in \mathbb{C}^{2 \times 2}$  as the polarimetric amplitude matrix

$$\mathbf{A}_{\ell}(f, t) = \begin{bmatrix} \alpha_{\ell}^{aa}(f, t) & \alpha_{\ell}^{ab}(f, t) \\ \alpha_{\ell}^{ba}(f, t) & \alpha_{\ell}^{bb}(f, t) \end{bmatrix} \quad (5)$$

where  $L$  is the total path number,  $\tau_{\ell}$  and  $\nu_{\ell}$  indicate the propagation delay and Doppler frequency for the  $\ell$ th path,  $a$  and  $b$  represent the polarization pair of the transmit and receive antennas, and  $\alpha_{\ell}^{\diamond\star}$  are the complex amplitudes for transmitted polarization  $\diamond$  and received polarization  $\star$ . Furthermore,  $\mathbf{k}_{\ell}^{\text{Tx/Rx}}$  is the wave vector in the departure/arrival direction at the Tx/Rx side for the  $\ell$ th path, and  $\mathbf{G}_{\text{Tx}} \in \mathbb{C}^{N \times 2}$  and  $\mathbf{G}_{\text{Rx}} \in \mathbb{C}^{M \times 2}$  represent the polarimetric antenna pattern matrices for Tx and Rx defined to a common phase center, respectively. Moreover, the first column and the second column in  $\mathbf{G}_{\text{Tx}}$  (and  $\mathbf{G}_{\text{Rx}}$ ) are antenna pattern vectors of  $a$  and  $b$  polarizations, respectively. With uplink transmission considered, we have  $\mathbf{G}_{\text{Tx}} \in \mathbb{C}^{M \times 2}$  and  $\mathbf{G}_{\text{Rx}} \in \mathbb{C}^{N \times 2}$ . Note that (4) is based on the assumption of plane-wave propagations. When considering spherical wavefronts [21], [30], [31], the model gets more complicated as the polarimetric complex gain of one path varies among antenna elements, and the Doppler frequency also change with respect to different antenna pairs. The spherical wavefront is out of the scope of this paper. Readers are referred to [21], [30]–[32] for the corresponding spherical-propagation models.

The purpose of channel emulation is to reproduce the MIMO channel, i.e. the channel transfer matrix  $\mathbf{H}$ , in a controllable and repeatable way in laboratory to test devices. In traditional conducted MIMO emulation, the Tx antenna ports and Rx antenna ports are connected to the input ports and output ports of the channel emulator, respectively. The channel  $\mathbf{H}$  is generated in the fading emulator and multiplied with the input  $\mathbf{X}$ , and the resulting signal  $\mathbf{Y}$  is fed to the Rx device [18]. However, as explained in the introduction, conventional conducted testing is no longer applicable for mmWave devices

<sup>2</sup>Without loss of generality,  $u$  is omitted for the sake of conciseness.

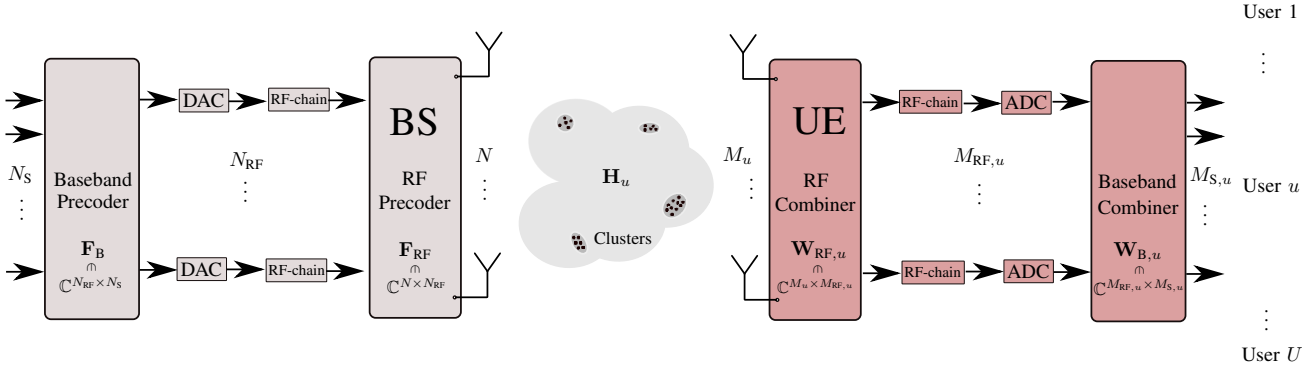


Fig. 1: System model of the wireless communication system.

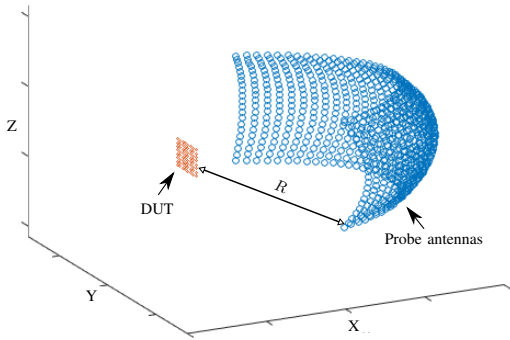


Fig. 2: Sectored probe configuration.

due to lack of antenna connectors. Highly integrated RF circuits and antenna designs are inevitable at mmWave bands due to concern of cost, size and loss. Alternatively, OTA testing by exploiting SMPAC method has been considered as the most appropriate strategy for the performance evaluation of mmWave massive MIMO devices.

### C. SMPAC OTA Emulation

The enhanced beamforming capacity in 3D (both azimuth and elevation) is advantageous to overcome the high path loss in mmWave bands and mitigate the interference among users. This in turn requires the OTA emulation to support 3D propagation, thus the 2D probe configuration [13], [33] applied for LTE 4G communications is no longer adequate for mmWave Massive MIMO devices. A SMPAC setup was thus first proposed in [18] as illustrated in Fig. 2. A large number of probes with approximately the same distance  $R$  to the DUT at the coordinate center and certain angle spacings among them are used to cover a sector of the whole sphere. This is based on the reasonable assumption that the propagation paths of mmWave propagations are confined in a certain angle-range/sector for most scenarios, and the hardware cost can be decreased with less probes used. In other words, the SMPAC setup is a compromise between the requirement of

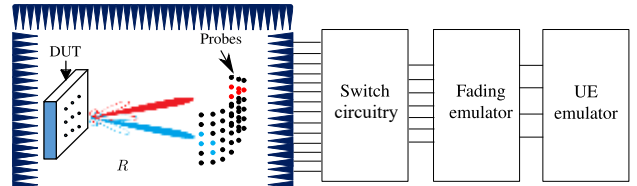


Fig. 3: A SMPAC system setup.

3D emulation and the hardware cost. As illustrated in Fig. 3, we exemplify the underlying mechanism for the SMPAC emulation by the uplink transmission where the DUT (Rx) is BS and Tx is the UE (or UE emulator). The setup contains an anechoic chamber, a number of probes with  $K$  of them active, a fading emulator, a UE emulator and a switch matrix to connect the  $K$  output ports of the fading emulator to the desired  $K$  active probes. In this setup, the channel transfer function  $\mathbf{H}$  is mainly reproduced by exploiting the fading emulator and probe configuration. Specifically, the channel transfer function  $\mathbf{H}_{re}$ , reproduced by the setup is formatted as

$$\mathbf{H}_{re}(f, t) = \mathbf{C}(f, t)\mathbf{E}(f, t) \quad (6)$$

where  $\mathbf{C} \in \mathbb{C}^{N \times K}$  is the channel transfer matrix due to the chamber from  $K$  probes to the  $N$  DUT antennas, and  $\mathbf{E} \in \mathbb{C}^{K \times M}$  is the channel transfer matrix attributed to the fading emulator between the  $M$  ( $M_u$ ) UE antennas and the  $K$  probes.

With the geometrical distribution of the  $K$  probes and  $N$  DUT antennas known, the  $(n, k)$ th element  $C_{n,k}$  of  $\mathbf{C}$  is determined as

$$C_{n,k}(f) = \mathbf{G}_{\text{Rx},n}(f, -\mathbf{k}_{n,k})\mathbf{G}_k^T(f, \mathbf{k}_{n,k}) \times \sqrt{PL(f, d_{n,k})} \exp\{-j\|\mathbf{k}_{n,k}\|d_{n,k}\} \quad (7)$$

where  $\mathbf{G}_{\text{Rx},n} \in \mathbb{C}^{1 \times 2}$  and  $\mathbf{G}_k \in \mathbb{C}^{1 \times 2}$  are the polarimetric antenna radiation patterns for the  $n$ th DUT antenna and the  $k$ th probe, respectively, and  $\mathbf{k}_{n,k}$ ,  $d_{n,k}$  and  $PL(f, d_{n,k})$  are the wave vector, distance and path loss of the propagation between the  $k$ th probe and the  $n$ th DUT antenna, respectively. It is worth noting that due to the propagation between the  $k$ th probe and the  $n$ th DUT antenna is line-of-sight, the polarization matrix is an identity matrix thus omitted in (7), and that the

time dependence of  $\mathbf{C}$  can be obtained from the distribution variation of selected  $K$  probes. By properly selecting the probe locations, the required PAS of the channel can be generated.

Since the temporal and Doppler characteristics of the channel cannot be embedded in  $\mathbf{C}$ , they are created by the fading emulator. The channel transfer matrix  $\mathbf{E}$  executed in the fading emulator has the property that its  $k$ th row  $\mathbf{E}_k$  can be formatted as

$$\mathbf{E}_k(f, t) = \sum_{\ell=1}^L w_{\ell,k} \mathbf{G}_{\text{FE},k} \mathbf{A}_{\ell,k} \mathbf{G}_{\text{Tx}}^T(f, \mathbf{k}_{\ell}^{\text{Tx}}) \times \exp\{j2\pi\nu_{\ell}t\} \exp\{-j2\pi f\tau_{\ell}\} \quad (8)$$

where  $\mathbf{G}_{\text{FE},k} \in \mathbb{C}^{1 \times 2}$  is the polarimetric pattern configured for the  $k$ th probe in the fading emulator, and  $\mathbf{A}_{\ell,k}$  and  $w_{\ell,k}$  are the polarization matrix and weight of the  $\ell$ th path for the  $k$ th probe. By examining (8), it can be known that the temporal and Doppler characteristics of all the  $L$  paths are passed to all the  $K$  probes by including the term  $\exp\{j2\pi\nu_{\ell}t\} \exp\{-j2\pi f\tau_{\ell}\}$ . Meanwhile, the polarization characteristics are guaranteed by properly setting  $\mathbf{G}_{\text{FE},k}$  and  $\mathbf{A}_{\ell,k}$  in (8), which also depends on the  $\mathbf{G}_k$  in (7). More specifically, the polarization matrix of the  $\ell$ th path between UE and BS (DUT) passed by the  $k$ th probe can be obtained as

$$\mathbf{A}_{\text{re},\ell,k} = \mathbf{G}_k^T \mathbf{G}_{\text{FE},k} \mathbf{A}_{\ell,k}. \quad (9)$$

Since both the ranks of  $\mathbf{G}_k$  and  $\mathbf{G}_{\text{FE},k}$  are 1 and the rank of  $\mathbf{A}_{\ell}$  in (4) is usually 2, at least two probes are required to reproduce  $\mathbf{A}_{\ell}$  as  $(\mathbf{A}_{\text{re},\ell,k_1} + \mathbf{A}_{\text{re},\ell,k_2})$ . One direct example is to co-locate two linearly-polarized probes that serve two polarizations, respectively. In this case, both  $\mathbf{G}_{k_1}$  and  $\mathbf{G}_{\text{FE},k_1}$  can be  $[1, 0]$ , while both  $\mathbf{G}_{k_2}$  and  $\mathbf{G}_{\text{FE},k_2}$  can be  $[0, 1]$ , and  $\mathbf{A}_{\ell,k_1/k_2}$  can be  $\mathbf{A}_{\ell}$ . Moreover, as different paths have different angle of arrivals, the weights  $\mathbf{W}_{\ell} = \{w_{l,k}; k = 1, \dots, K\}$  are optimized together with the locations of the  $K$  probes to control the spatial characteristics.

Ideally, to exactly reproduce  $\mathbf{H}$ , one can execute  $\mathbf{E}$  in the fading emulator as

$$\mathbf{E} = \mathbf{C}^{-1} \mathbf{H}. \quad (10)$$

However, the difficulty lies in the fact that  $\mathbf{C}$  is typically non-measurable, e.g., due to the hybrid structure. Moreover, what matters is the statistical behaviour of the geometry-based stochastic channel rather than its instantaneous snapshots [18]. Alternatively, the purpose is to reproduce a statistically similar  $\mathbf{H}_{\text{re}}$  to  $\mathbf{H}$ . As discussed above, the statistical behaviour in the temporal, Doppler and polarization domains can be mostly executed in the fading emulator, the challenge is to control the statistical spatial behaviour in the anechoic chamber. This is achieved by properly choosing the  $K$  probes and setting  $\mathbf{W}_{\ell}$ . Prefaded signal synthesis (PFS) [13], [14] and plane wave synthesis (PWS) [15]–[17] approaches can be applied, between which PFS is preferable and exploited in this work as the PWS requires strict phase coherence to emulate plane-waves in the test-zone.

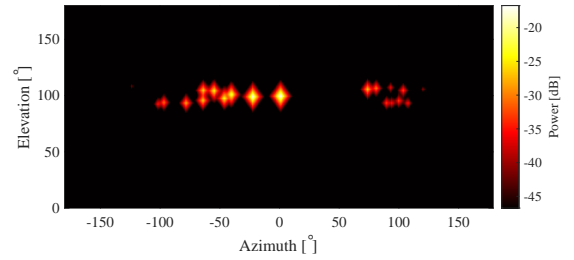


Fig. 4: The PAS of CDL C.

#### D. Beamforming Effect on the Channel Emulation

In massive MIMO communications, both beamforming and spatial multiplexing can be exploited. We distinguish the two terms the same way as in [3]. That is, beamforming indicates a classically steered beam, while spatial multiplexing indicates that an outgoing signal stream is divided into independent substreams and sent in parallel through the same radio channel. It can, for both theoretical and practical reasons, be argued that beamforming will be applied predominantly in mmWave massive MIMO communications. *i)* Numerous channel measurement campaigns have shown that the high attenuation at mmWave bands mostly results in power-limited channels. Beamforming is thus necessary to provide sufficient link budget [3], [34], and larger capacity could be achieved with higher order modulations due to increased SNR [3]. *ii)* It is usually required for spatial multiplexing that the channel state information (CSI) is available at the Tx side. However, the hybrid structure and large number of antennas pose significant challenges and overheads in CSI acquisition [3], [27]. Alternatively, beam management with beamforming aiming to select the best beam pair between a BS and a UE requires less and easier feedback, e.g. as proposed in the 3rd Generation Partnership Project (3GPP) standard [29], [34]. *iii)* Due to hardware limitations, it can be expected that the analog structure is preferable for UEs in the early evolution of mmWave communication systems. This further hinders the application of spatial multiplexing for a single user.

It is clear that in the beamforming mode, the propagation channel will be spatially filtered. That is, although multiple clusters may exist in the channel, the directed and narrow beam makes clusters in the other directions insignificant to the communication link. Nevertheless, it is worth noting that clusters fade independently. If the DUT is in beam tracking mode, i.e., following several clusters and always tracking the strongest one, the beam may not be always directed to the cluster with a maximum-power PAS. Thus, there may be one or several clusters that can be considered dominant, and they should not be pruned in OTA emulation. To illustrate the effect of beamforming on mmWave channels, five different representative 3GPP clustered-delay-line (CDL) models (A-E) specified in [19] are exploited, where models D-E and A-C correspond to line-of-sight (LoS) and non line-of-sight (NLoS) scenarios, respectively. As an example, the PAS of CDL model C is illustrated in Fig. 4. Since it is important to evaluate the beam management performance and the throughput of the DUT, the beam allocation distribution and the mean power

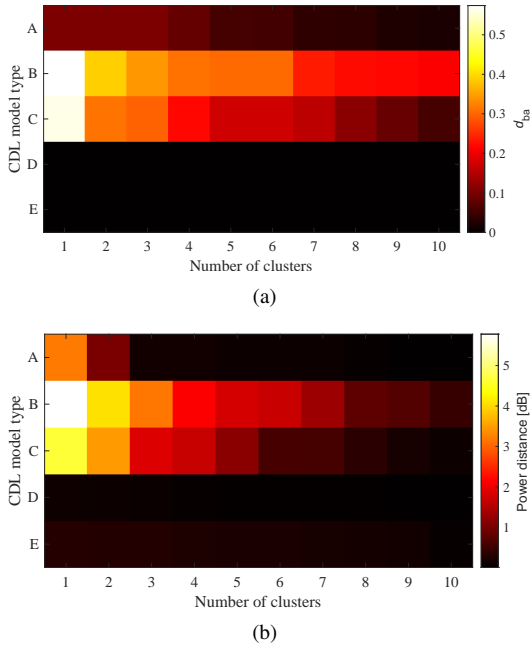


Fig. 5: The evaluation of the number of dominant clusters for an  $8 \times 8$  DUT array with beamforming. (a) Total variation distance of beam allocation distributions. (b) Mean power difference of directed beams.

of all directed-beams<sup>3</sup> are used respectively to compare the original channel and the pruned channel with different number of dominant clusters included. Specifically, the *total variation distance of beam allocation distributions* [see Sect. III-B(3)] and the distance of the mean powers are calculated for each of the five scenarios considering an  $8 \times 8$  DUT array. As illustrated in Fig. 5, it can be observed that the LoS path only is always enough for the LoS channel scenarios D-E. However, for the NLoS channel scenarios, several dominant clusters are needed to achieve a satisfactory emulation performance. For example for CDL A, one or two dominant clusters are quite fine. For CDL C, five clusters may be needed. Since the channel can be pruned by considering only the dominant cluster(s), it is important to reproduce each cluster as accurately as possible especially when they are evolving in the angular domain in dynamic scenarios. In the sequel, investigations on how to accurately emulate a dynamic cluster are elaborated. Multiple clusters can be emulated together by emulating individual dynamic clusters accurately. Compared to the method of emulating the composite channel as a whole, the proposed method emphasizes the emulation accuracy of a few dominant clusters (if not one), which is important for mm-wave massive MIMO communications and also saves expensive resources. Moreover, the dynamic behavior of a cluster can be well considered.

### III. SMPAC DESIGN FOR OTA CHANNEL EMULATION

In this section, probe allocation and weighting in SMPAC setup are discussed first. Four metrics (including total variation

<sup>3</sup>Directed beam means the beam with the maximum power during beam sweeping.

distance of PAS, spatial correlation error, beam peak distance and total variation distance of beam allocation distributions) are then used in the simulation to evaluate how the SMPAC design parameters, e.g., probe number and angle spacing, affect the emulation performance for a single-cluster channel. Moreover, a novel cost-effective design for probes and switching strategy is discussed to emulate the dynamic channels.

#### A. Probe Allocation and Weighting

In PFS, independent and identically distributed (i.i.d.) fading sequences (e.g. Rayleigh distribution [13]) are generated at the selected  $K$  probes. By applying probe weights  $w_k$  for each of the  $K$  probes, it is expected to reproduce the target PAS  $P(\Omega)$ .<sup>4</sup> The weights  $w_k, k = 1, \dots, K$  are obtained by minimizing the square error between the target spatial correlations and reproduced spatial correlations. Specifically, with a target PAS  $P(\Omega)$ , the spatial correlation between any two (the  $a$ th and  $b$ th) DUT antennas can be formatted as

$$\rho_{a,b} = \frac{\oint P(\Omega) \exp\{j\mathbf{k}_\Omega \cdot (\mathbf{a} - \mathbf{b})\} d\Omega}{\oint P(\Omega) d\Omega} \quad (11)$$

where  $\mathbf{a}$  and  $\mathbf{b}$  are the location vectors for the  $a$ th and  $b$ th DUT antennas, respectively, and  $\mathbf{k}_\Omega$  is the wave vector in the direction of space angle  $\Omega$ . With  $K$  probes selected, the reproduced spatial correlation between the  $a$ th and  $b$ th DUT antennas can be calculated as [13], [18]

$$\hat{\rho}_{a,b} = \frac{\sum_{k=1}^K w_k^2 PL(d_{a,k}) PL(d_{b,k}) \exp\{j\|\mathbf{k}\|(d_{a,k} - d_{b,k})\}}{\sqrt{\sum_{k=1}^K w_k^2 PL^2(d_{a,k}) \sum_{k=1}^K PL^2(d_{b,k})}} \quad (12)$$

The numerator in (12) can give some insight that the cross terms have to vanish with i.i.d. fading sequences applied for different probes, and the denominator in (12) is simply a normalization factor. The optimized  $\mathbf{W}$  is then obtained by minimizing the square error between the target correlation function and the reproduced correlation function as

$$\mathbf{W} = \arg \min_{\mathbf{W}} \sum_{a=1}^N \sum_{b=1}^N |\rho_{a,b} - \hat{\rho}_{a,b}|^2. \quad (13)$$

It is worth noting that the probe weighting and allocation are actually a joint optimization problem. In this work, we attempt to select the best  $K$  probes within two steps. First, a relatively large probe area is considered active for the SMPAC emulation, and their weights are calculated according to (13). Then the probes with the  $K$  highest  $|w_k|^2$  are selected to be active only, and the weights for the  $K$  probes are optimized again using (13).

#### B. Performance Evaluation Metrics

The critical SMPAC design parameters include the range  $R$  between DUT and probes, the angular spacing  $\theta_s$  of probes seen from test zone, the number of selected probes  $K$  and the angular coverage of the probe panel seen in test zone. To determine the range  $R$ , two issues have to be considered.

<sup>4</sup>Note that the subscript  $\ell$  is omitted in  $w_{\ell,k}$  because the weights for different paths in the same cluster should be the same.

One is the link budget that determines the upper-bound of  $R$ . The other is the spherical curvature effect that determines the lower-bound of  $R$ . Readers can refer to [35] for detailed discussion on the determination of  $R$  for different bands at 2.6, 3.5 and 28 GHz, where several parameters including the fixed beam power loss are introduced to investigate the spherical curvature effect. It is worth noting that in the mmWave frequency bands, the far-field distance gets smaller as wavelength decreases. For example, the Fraunhofer far-field distances [21], [31] for a  $16 \times 16$  and an  $8 \times 8$  DUT array (planar and uniformly half-wavelength spaced) at 28 GHz are calculated as 0.60 and 0.13 m, respectively.<sup>5</sup> It is thus reasonable to assume that the curvature effect is insignificant with a proper setting of range length. In addition, it has been concluded in [35] that the Fraunhofer distance is not a precondition for  $R$  in fading testing. In this regard, we do not consider the metrics for evaluating  $R$  in this study, and a practical range length, i.e. 2 m, is set for the investigations in the sequel. To evaluate the OTA emulation performance with different settings of probe number and angular spacing, four evaluation metrics introduced in [18] are adopted. For the sake of completeness, definitions of the four metrics are briefly included as follows.

1) *Spatial Correlation Error*  $e_\rho$ : This parameter  $e_\rho$  is to compare the target PAS and the emulated PAS by comparing the target spatial correlation and the emulated spatial correlation, which is formatted as

$$e_\rho = \sqrt{\frac{1}{N^2} \sum_{a=1}^N \sum_{b=1}^N |\rho_{a,b} - \hat{\rho}_{a,b}|^2 \max(|\rho_{a,b}|, |\hat{\rho}_{a,b}|)}. \quad (14)$$

Note that the weight  $\max(|\rho_{a,b}|, |\hat{\rho}_{a,b}|)$  is applied for emphasizing the deviation of a large correlation coefficient. The reason is that a correlation deviation of a large correlation coefficient has more significant impact than that of a small correlation coefficient [18].

2) *Total Variation Distance of PAS*  $d_p$ : Similar to  $e_\rho$ , this parameter  $d_p$  is introduced as an alternative to compare the target and emulated PASs by comparing the obtained Bartlett beamforming spectra (normalized) of target and emulated channels. Specifically, the Bartlett beamforming spectra  $P_t$  and  $P_o$  for the target channel and the emulated channel respectively can be formatted as

$$P_{t/o}(\Omega) = \mathbf{a}^H(\Omega) \mathbf{R}_{t/o} \mathbf{a}(\Omega) \quad (15)$$

where  $\mathbf{R}_{t/o} \in \mathbb{C}^{N \times N}$  is the covariance matrix with its  $(a, b)$ th element equal to the unnormalized  $\rho_{a,b}$  in (11) for  $\mathbf{R}_t$  and the unnormalized  $\hat{\rho}_{a,b}$  in (12) for  $\mathbf{R}_o$ , and  $\mathbf{a}$  is the steering vector.

<sup>5</sup>The minimum far-field distance is calculated according to  $\frac{2D^2}{\lambda}$ , where  $D$  is the diameter of the smallest sphere that encloses the radiating elements of the DUT. However, the exact antenna size of the DUT is usually unknown, and the radiating aperture is also determined by the ground coupling effects. If the DUT is viewed as a “black-box”, the largest device dimension could be utilized. Using this “black-box” approach is overkilling and may bring up unnecessary costs on testing hardware, because antennas can only be placed in limited area, e.g., in several possible locations of a device and its configuration complexity is significantly constraint in practice. In this paper, the “white-box” approach focusing only on the radiating elements is adopted for simplicity and authenticity.

The total variation distance of PAS is then calculated as

$$d_p = \frac{1}{2} \int \left| \frac{P_t(\Omega)}{\int P_t(\Omega') d\Omega'} - \frac{P_o(\Omega)}{\int P_o(\Omega') d\Omega'} \right| d\Omega. \quad (16)$$

This can be interpreted as the difference between two 2D joint-distribution functions. The value of  $d_p$  ranges between  $[0, 1]$ , with 0 indicating full similarity and 1 full dissimilarity.

3) *Total Variation Distance of Beam Allocation Distributions*  $d_{ba}$ : For the 5G devices performing beam operations such as beam sweeping and refinement [29], [34], several beams with indices  $\{1, \dots, B\}$  are pre-defined, and the one with the maximum power is selected. For a stochastic channel with a certain PAS, the probability of the  $b$ th beam is selected should be a certain value. In other words, there is a certain beam allocation distribution for the target channel which indicates each beam’s selection probability. The parameter  $d_{ba}$  is exploited to calculate the distance between the beam allocation distributions  $p_t$  and  $p_o$  of the target and emulated channels as

$$d_{ba} = \frac{1}{2} \sum_{b=1}^B |p_t(\Omega_b) - p_o(\Omega_b)| \quad (17)$$

where  $\Omega_b$  is the steered direction of the  $b$ th pre-defined beam. It can be known that the value of  $d_{ba}$  is between  $[0, 1]$  with 0 indicating the same distribution.

4) *Beam Peak Distance*  $d_{bp}$ : This parameter is similar to  $d_{ba}$ , which is used to compare the expected beam directions of  $p_t$  and  $p_o$  as

$$d_{bp} = \left| \sum_{b=1}^B \Omega_b p_t(\Omega_b) - \sum_{b=1}^B \Omega_b p_o(\Omega_b) \right|. \quad (18)$$

In the sequel, investigations on probe number and angular spacing of probes are conducted using the above four parameters as evaluation criteria.

### C. Numerical Investigations

In this section, simulations are implemented to investigate how different numbers of probes and angular spacing affect the one-cluster channel emulation performance for DUTs of different sizes. Specifically, half-wavelength spaced uniform planar arrays at 28 GHz are considered with fixed array element (isotropic radiation pattern) and array dimensions ranging from  $2 \times 2$  to  $16 \times 16$ . The probe number  $K$  is set to change from 1 to 10, and the angular spacing  $\theta_s$  is set to vary from  $1^\circ$  to  $20^\circ$ . The range  $R$  is fixed to 2 m as discussed in Sect. III-B. Moreover, the azimuth and elevation spreads of the cluster are set to  $5^\circ$  and  $3^\circ$ , respectively, and the cluster PAS obeys the Laplace distribution as standardized in [19]. Table I summarizes the simulation parameters.

In a realistic channel, the dominant cluster usually evolves in the spatial domain. In other words, the channel is dynamic and spatially consistent (e.g., see the realistic indoor channel presented in Sect. IV). Therefore, it is essential that the emulation system can handle the dynamic behaviors with spatial evolution. As illustrated in Fig. 6, it can be observed that

Table I: OTA parameters applied in the simulations

Simulation parameters			
Probe number $K$	[1:10]	Center frequency	28 GHz
Angular spacing $\theta_s$	[1:20]	Cluster azimuth spread	5°
DUT array dimension	2×2 to 16×16	Cluster elevation spread	3°
DUT beam sweeping	DUT HPBW	Cluster PAS distribution	Laplace
Range length $R$	2 m	Cluster cases	Aligned/far-nonaligned

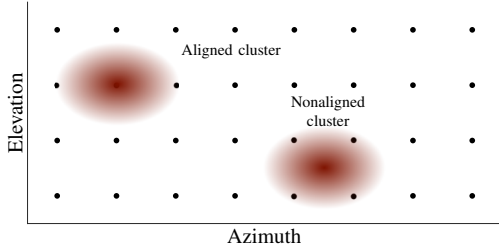


Fig. 6: An illustration of aligned and nonaligned cases when cluster evolves in angular domain.

during the cluster evolution in angular domain, it is possible that the cluster’s centroid would align with a probe and also aloof from all probes. We denote them as “aligned” case and “nonaligned” case, respectively. It is intuitive that the PAS may be better generated with less probes in the aligned-case. However, it may be more difficult to mimic the target PAS distribution in the non-aligned-case where there is no probe existing at its distribution center, especially in the “far-nonaligned” case where the cluster centroid is in the center of a neighbouring four-probes as indicated in Fig. 6. Thus, the two very different cases are further considered in the simulation. Another issue needs to be considered in the simulation is how to sweep beams (determine the angular spacing of the beam sweeping), which is related to the calculation of  $d_{ba}$  and  $d_{bp}$ . In the simulation, it is set as the half-power-beamwidth (HPBW) of the DUT’s steering beams so that all the PAS power can be appropriately covered avoiding too much overlapping. In total 6000 ( $15 \times 10 \times 20 \times 2$ ) combinations are simulated considering array dimension, probe number, angular spacing and the two cluster-evolution cases. For each combination, the four performance evaluation metrics as elaborated in Sect. III-B are calculated. Due to the space limitation, representative figures for the results of three different DUT dimensions, i.e.,  $2 \times 2$ ,  $8 \times 8$  and  $16 \times 16$ , are presented. The  $2 \times 2$  is considered as a typical UE device,  $8 \times 8$  a typical BS array, and  $16 \times 16$  a device with enhanced capability.

1) *Aligned cluster case:* Figs. 7-9 illustrate the four performance evaluation metrics corresponding to different probe number  $K$  and angular spacing  $\theta_s$  in the case of aligned cluster for a  $2 \times 2$ ,  $8 \times 8$  and  $16 \times 16$  DUT array, respectively. It can be observed from Fig. 7 that the four performance evaluation metrics are sufficiently small for all  $K$ - $\theta_s$  pairs. This demonstrates that one probe is adequate to emulate one cluster for a  $2 \times 2$  DUT array. It is reasonable because the beam resolution of this array is limited, and the cluster spread at mmWave bands is usually small. With a probe existing at the centroid of the cluster, the PAS can be well emulated

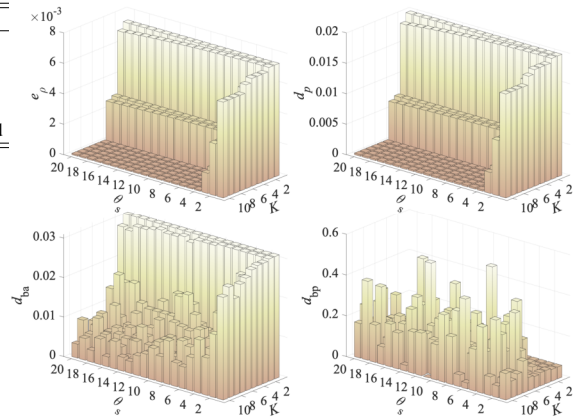


Fig. 7: SMPAC OTA emulation performance for a  $2 \times 2$  DUT array with different numbers of probes and angular spacing in aligned cluster case.

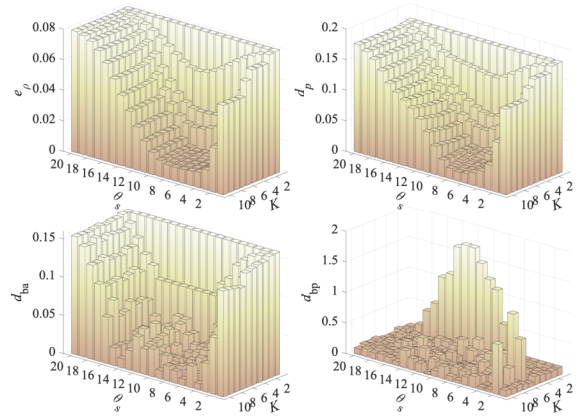


Fig. 8: SMPAC OTA emulation performance for an  $8 \times 8$  DUT array with different numbers of probes and angular spacing in aligned cluster case.

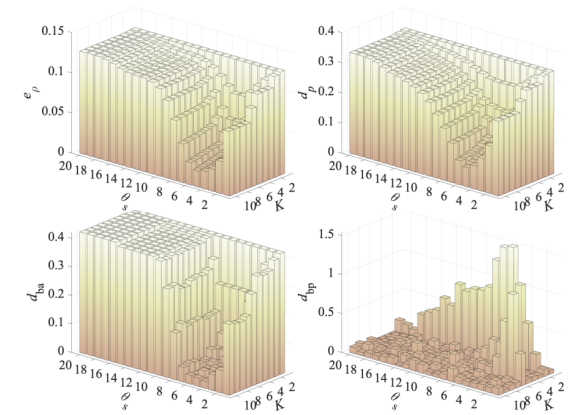


Fig. 9: SMPAC OTA emulation performance for a  $16 \times 16$  DUT array with different numbers of probes and angular spacing in aligned cluster case.

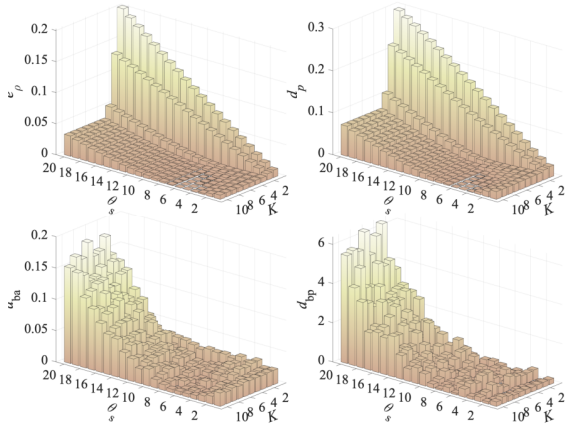


Fig. 10: SMPAC OTA emulation performance for a  $2 \times 2$  DUT array with different numbers of probes and angular spacings in far-nonaligned cluster case.

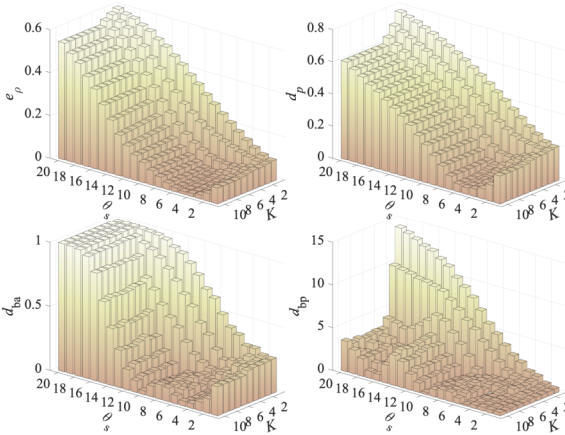


Fig. 11: SMPAC OTA emulation performance for an  $8 \times 8$  DUT array with different numbers of probes and angular spacings in far-nonaligned cluster case.

for the DUT array. As illustrated in Fig. 8, the performance degrades for an  $8 \times 8$  array, since its ability to resolve different propagation paths is better compared to the  $2 \times 2$  array. This is similarly true for the  $16 \times 16$  DUT array where the performance degrades with the same  $K$ - $\theta_s$  compared to that of  $2 \times 2$  and  $8 \times 8$  arrays. Nevertheless, it can be observed from Figs. 7-9 that the performances for the three DUTs are still decently well even though only one probe is deployed, as indicated by the maximum values of  $e_p$ ,  $d_p$ , and  $d_{ba}$  under 0.4. It is due to the fact that a probe is aligned to the cluster. Moreover, a common pattern can be observed from Figs. 7-9. That is, the best performance is obtained with a moderate angular spacing. In other words, when  $\theta_s$  is too small or too large, the performance degrades. The reason is that with a too small  $\theta_s$ , the emulated power is too concentrated; while with a too large  $\theta_s$ , probes except the aligned one are far away from the main paths of this cluster. Both two cases result in a bad emulation for the PAS distribution.

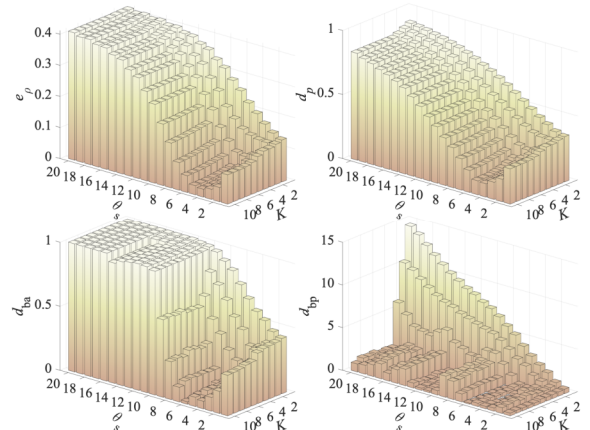


Fig. 12: SMPAC OTA emulation performance for a  $16 \times 16$  DUT array with different numbers of probes and angular spacings in far-nonaligned cluster case.

2) *Far-nonaligned cluster case*: Figs. 10-12 illustrate the four performance evaluation metrics corresponding to different probe number and angular spacing in the case of far-nonaligned cluster for a  $2 \times 2$ ,  $8 \times 8$  and  $16 \times 16$  DUT array, respectively. Different from the aligned cluster case, it can be observed from Figs. 10-12 that the errors/distances between the target and the emulated metrics for the non-aligned cluster case are obviously larger (e.g. see the values with one probe where PAS). This is reasonable due to the fact the cluster centroid is far away from any probes, and a better emulation of the PAS requires more probes compared to that of the aligned cluster case. Moreover, similar observations as the aligned cluster case can be appreciated from Figs. 10-12 as follows. A larger sized DUT requires more probes and smaller angular spacing to gain similar performance to that of a smaller sized DUT. With the same angular spacing, a larger number of probes can result in a better performance. However, with the same probe number, a moderate angular spacing is preferable.

To provide guidelines for selecting proper  $K$  and  $\theta_s$ , upper-bounds are defined for the four performance evaluation metrics. With certain predefined bounds, multiple  $K$ - $\theta_s$  pairs may meet the requirements. Among all the candidates, the pairs with the smallest  $K$  are firstly searched, and then the pair with the largest  $\theta_s$  is finally chosen as a “good” option, since it is reasonable to assume the fading emulator resource is much more expensive, and a larger  $\theta_s$  can result in a larger angular coverage. Table II summarizes the recommended (“good”) options for the different DUTs and different bounds. Note that the following three aspects are considered when generating this table. *i)* Both aligned and nonaligned conditions are considered. *ii)* Beam peak distance  $d_{bp}$  is not considered because its value is not confined in a certain range as the other three metrics in  $[0,1]$ , and it is related to  $d_{ba}$ . *iii)* It is possible that one metric slightly exceeds its upper bound, yet other metrics are well under their corresponding bounds. Thus a soft total bound is applied. That is, a setup is considered a candidate if the sum of the metrics’ values are smaller than the

Table II: OTA setup recommended for different DUTs and for different performance levels.

$(K, \theta_s [^\circ])$ \ DUT	2×2	3×3	4×4	5×5	6×6	7×7	8×8	9×9	10×10	11×11	12×12	13×13	14×14	15×15	16×16
0.10×3	(1, 10)	(1, 6)	(1, 4)	(1, 2)	(2, 1)	(3, 7)	(3, 7)	(4, 8)	(4, 7)	(4, 6)	(4, 6)	(4, 6)	(4, 6)	(4, 5)	(5, 5)
0.15×3	(1, 16)	(1, 10)	(1, 7)	(1, 5)	(1, 4)	(1, 2)	(1, 1)	(3, 8)	(3, 7)	(3, 6)	(3, 6)	(4, 7)	(4, 6)	(4, 6)	(4, 6)
0.20×3	(1, 20)	(1, 14)	(1, 10)	(1, 7)	(1, 6)	(1, 4)	(1, 4)	(1, 1)	(2, 5)	(2, 5)	(2, 5)	(3, 5)	(3, 5)	(3, 5)	(3, 5)
0.25×3	(1, 20)	(1, 17)	(1, 12)	(1, 10)	(1, 8)	(1, 6)	(1, 5)	(1, 3)	(1, 3)	(1, 3)	(1, 2)	(3, 6)	(3, 6)	(3, 6)	(3, 6)
0.30×3	(1, 20)	(1, 20)	(1, 15)	(1, 12)	(1, 9)	(1, 7)	(1, 7)	(1, 4)	(1, 4)	(1, 4)	(1, 4)	(2, 4)	(2, 4)	(2, 4)	(2, 4)

sum of their bounds. For example, 0.1×3 in Table II indicates the soft bound by summing the three bounds (all set as 0.1) of  $e_p$ ,  $d_p$  and  $d_{ba}$ . It can be observed from Table II that with a larger upper bound, basically less probes and/or a larger angular spacing can be applied. For a typical 8×8 BS DUT array at 0.1×3 soft bound, (3, 7°) is recommended, and for a 16×16 DUT array (5, 5°) is recommended which can be considered as a setup applicable for all DUTs.

### 3) A cost-effective design principle for dynamic cluster emulation:

Since the number of active probes required for emulating a cluster is limited, and the active probes are confined in a compact angular area, it is unnecessary to use a switch matrix with full freedom. Alternatively, several 1-to- $Q$  switches each connecting to an output port of the fading emulator can be utilized. Fig. 13 exemplifies the proposed design strategy, where 4 probes ( $K = 4$ ) are active; in other words, the fading emulator provides 4 output ports. An 1-to- $Q$  switch ( $Q = 4$  in the example) is connected to each output port, and each output port can activate one of the  $Q$  probes at one time instant. Totally  $KQ$  probes are installed on the panel in an interleaved style as sketched in Fig. 13. With such a design the four output ports can follow a dynamic cluster by activating the necessary probes, e.g. as indicated by the dashed squares in Fig. 13. The angular coverage can be increased by increasing  $Q$ . With azimuth and elevation coverage required as  $\theta_A$  and  $\theta_E$  respectively,  $Q$  can be approximately calculated as

$$Q = \left\lceil \frac{\lceil \frac{\theta_A}{\theta_s} + 1 \rceil \cdot \lceil \frac{\theta_E}{\theta_s} + 1 \rceil}{K} \right\rceil \quad (19)$$

with  $\lceil x \rceil$  indicating the smallest integer larger or equal  $x$ . The advantage of this strategy compared to [18] is that a switch circuit with full freedom is replaced with several 1-to- $Q$  sub-switches (implemented e.g. using multistage 1-to- $Q'$  switches), thus significantly decreasing the complexity and cost.

To evaluate this setup, an artificial dynamic cluster is emulated for an 8×8 DUT array with  $K = 4$  and  $\theta_s = 8^\circ$ . The dynamic cluster centroid is set to evolve simultaneously and linearly from  $-60^\circ$  to  $60^\circ$  in azimuth and from  $-30^\circ$  to  $30^\circ$  in elevation within a few time snapshots. Figs. 14(a) and (b) illustrate the target PASs sliced in azimuth and elevation planes, respec-

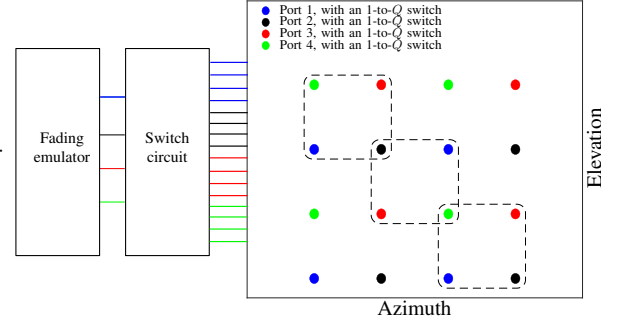


Fig. 13: An sketch of the proposed switch and panel design strategy.

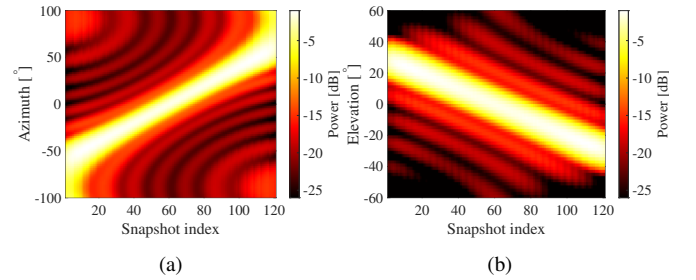


Fig. 14: Target dynamic PASs for the artificial dynamic channel. (a) Dynamic azimuth PAS. (b) Dynamic elevation PAS.

tively, while Figs. 15(a) and (b) the emulated ones.<sup>6</sup> Through intuitive visual inspection, the target and emulated dynamic PASs are quite similar. The quantitative similarity for azimuth plane is calculated as 96.7% ( $d_p=3.3\%$ ) using (16), and that for elevation PASs is calculated as 94.5%. This demonstrates that the dynamic channel has been emulated with decently good performance using the proposed switching strategy. It is worth noting that when the cluster is evolving between an aligned cluster and a non-aligned cluster using the same resource, the emulation spectra as illustrated in Fig. 15 are not very smooth since nonaligned-cluster snapshots are more resource-demanding.

<sup>6</sup>Note that the target or emulated PAS is a 3D spectrum in both azimuth and elevation domains at each time snapshot. It is not easy to plot/show the 3D spectrum dynamically evolving with respect to time. Alternatively, two slices of the 3D spectrum in azimuth and elevation planes respectively (like the E-plane and H-plane of an antenna pattern) are obtained at each time snapshot. By concatenating these slices with respect to the snapshot-index (time), the dynamic PASs are shown in Figs. 14 and 15.

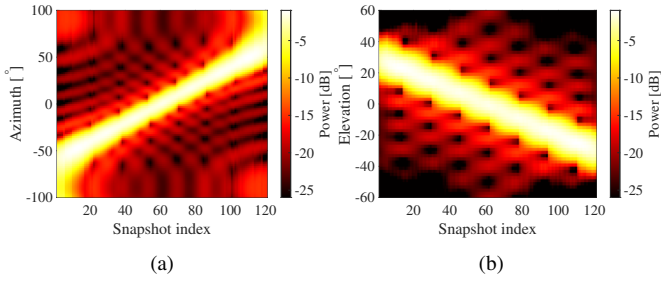


Fig. 15: Emulated PASs for the artificial dynamic channel. (a) Dynamic azimuth PAS. (b) Dynamic elevation PAS.

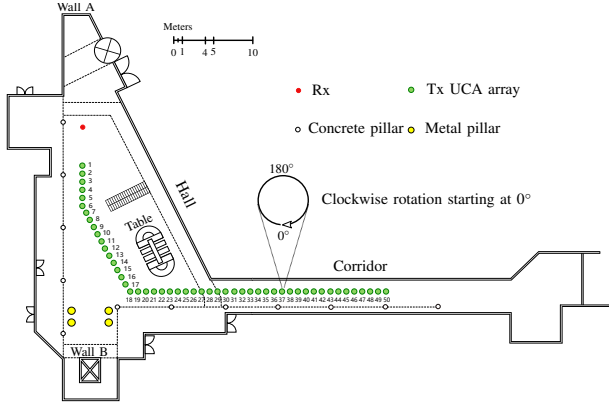


Fig. 16: The layout of the indoor measurement scenario.

#### IV. EMULATION VALIDATION USING A REALISTIC INDOOR DYNAMIC MMWAVE CHANNEL

In this section, an indoor measurement campaign is introduced. By exploiting a high-resolution channel parameter estimation algorithm as well as a clustering identification and tracking algorithm, dynamic clusters of the channel are extracted from the measurement data [20]. The dynamic evolution behavior of the dominant cluster are shown. Furthermore, the applicability of the proposed OTA setup is validated by the measure channel. This measurement campaign also sheds lights on how large the probe panel should be designed.

##### A. Measurement campaign and cluster tracking

An ultra-wideband measurement system developed based on a vector network analyzer (VNA) and the radio-over-fiber technique was applied in the measurement campaign. Phase coherent measurements can be done by exploiting the proposed phase compensation scheme using optical circulators. Furthermore, a dynamic range of 112 dB at 30 GHz can be obtained with an optical fiber of 300 m length due to its low attenuation to the signals. Readers are referred to [36] for the system details. The measurement campaign was conducted in an indoor hall-to-corridor scenario with its layout illustrated in Fig. 16 (Fig. 1(a) in [20]), and the ceiling height was about 10 m. Tables, stairs, metallic pillars, concrete pillars, etc. existed in the hall. Two quasi-omnidirectional bi-conical antennas were utilized as Tx and Rx antennas, respectively. The Rx antenna was fixed during measurement as indicated

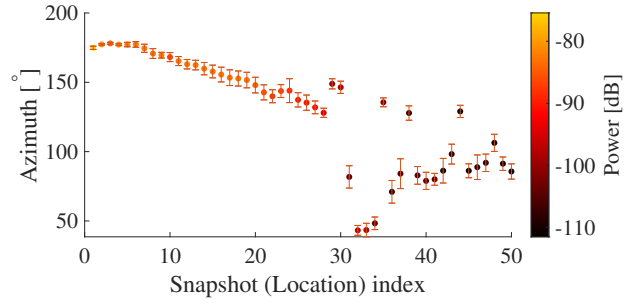


Fig. 17: The dynamic evolution of the dominant cluster for the indoor channel.

in Fig. 16, with a height of 3 m. The Tx antenna was installed on a rotator with a height of 1.15 m, and it was rotated in the azimuth plane with 360 uniform steps to perform a virtual uniform circular array (UCA) measurement where the circular radius was 0.25 m. In each step, channel transfer function (CTF) between Tx and Rx was measured using the VNA sweeping 2000 samples in the 28-30 GHz frequency band. Totally 50 UCA locations were measured from the hall to the corridor.

Based on the measured CTF at each UCA location, the propagation parameters of multipath components (MPCs), including propagation delays, azimuth angles, elevation angles and complex amplitudes, are estimated using a high-resolution estimation algorithm [21], [31]. Note that since the array measurement was applied only for one side, the angle information at the other side cannot be obtained. The underlying signal model of the channel impulse response can be formatted as

$$h(\tau, \phi, \theta, d) = \sum_{\ell=1}^L \alpha_{\ell} \delta(\tau - \tau_{\ell}) \delta(\phi - \phi_{\ell}) \delta(\theta - \theta_{\ell}) \delta(d - d_{\ell}) \quad (20)$$

where  $L$  is the total number of MPCs, and  $\alpha_{\ell}$ ,  $\tau_{\ell}$ ,  $\phi_{\ell}$ ,  $\theta_{\ell}$  and  $d_{\ell}$  represent the complex amplitude, propagation delay, azimuth, elevation and spherical wavefront distance of the  $\ell$ th MPC, respectively. Furthermore, based on the MPC estimation results, clusters of MPCs are grouped at each location by exploiting a threshold-based clustering algorithm, and dynamic clusters are associated across the 50 locations using a cluster tracking algorithm as proposed in [20]. For the MPC estimation, cluster identification and cluster tracking algorithms, readers are referred to [20], [21], [31] for more details.

##### B. OTA Emulation for the dynamic channel

Fig. 17 illustrates the dynamic evolution of the dominant cluster in azimuth domain obtained from the cluster identification and tracking results across the 50 locations, and the error bars indicate the azimuth spread at each location. The mean and standard deviation of the azimuth spread are calculated as  $4.7^{\circ}$  and  $2.2^{\circ}$ , respectively. It can be observed that in the hall scenario (locations 1-28), the dominant cluster is rather stable with relatively high power. It is actually the LoS cluster. After entering into the corridor, the LoS cluster was blocked, and the dominant cluster changed abruptly to another NLoS

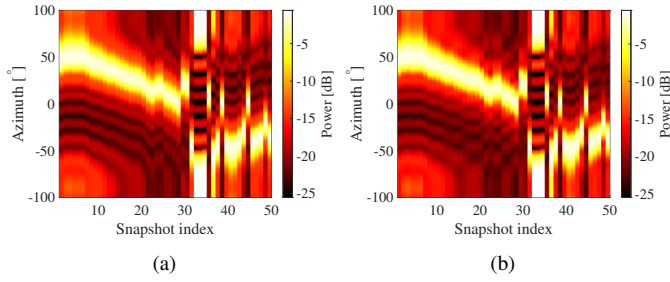


Fig. 18: Target and emulated dynamic PAS for the measured indoor channel. (a) Target azimuth PAS. (b) Emulated azimuth PAS.

ones with very different azimuths. Furthermore, the cluster was with much weaker power, and its evolution was less stable than that of LoS cluster. This demonstrates that beam tracking is essential for the device to track promptly the change of the dominant cluster. Meanwhile, beamforming is critical to mitigate the attenuation to achieve acceptable link budget at mmWave frequency bands especially in the NLoS case (corridor). All these put significant importance on the channel emulation of the realistic channels for performance evaluation. Figs. 18(a) and (b) illustrate the target indoor azimuth PAS and emulated azimuth PAS by exploiting the setup with  $K = 4$  and  $\theta_s = 8^\circ$  for an  $8 \times 8$  DUT array. Note that the cluster power has been normalized at each location. It can be observed that the two PASs are similar, and the similarity defined as  $1 - d_p$  [see (16)] is calculate to be 98.2%. It is worth noting that the azimuth coverage of the panel should be at least around  $150^\circ$  since the dominant cluster changed in a azimuth range of around  $150^\circ$  as illustrated in Fig. 17. Moreover, it can be observed that the cluster azimuth range was not centered at  $0^\circ$ , thus a pre-rotation should be applied to the device to make the center of the dominant cluster's angle range align with the probe panel center.

## V. CONCLUSIONS

In this paper, a dynamic mmWave channel emulation method for 5G mmWave massive MIMO devices in a sectored multiprobe anechoic chamber (SMPAC) setup was investigated. We exploited the fact that with beamforming, only a few dominant clusters or even one dominant cluster have to be considered in the OTA emulation. Based on this dominant-clusters concept, a cost-efficient OTA emulation strategy for dynamic mmWave channels was proposed. That is, we focused on reproducing the dominant cluster(s) with high accuracy rather than the composite channel. A switch-circuit with low cost profile using interleaved probes that belong to different 1-to-multiple sub-switches was also designed for this purpose. Comprehensive simulations demonstrated that 4 probes are adequate to simulate the dynamic mmWave channels with high accuracy (errors below 0.1) considering the dominant-cluster properties, although the optimized angular spacing among probes needs to be set with respect to particular DUT size (see Tabel II). Moreover, the dynamic mmWave channel measured in an

indoor scenario showed that the dominant cluster evolved in a relatively large azimuth range (i.e. around  $150^\circ$ ) and presented abrupt changes, and its mean azimuth spread was observed to be around  $4.5^\circ$ . The proposed SMPAC setup was able to emulate the dynamic behaviors of the measured reality with high accuracy, which further validated the proposed strategy. This work can serve as a certain guideline for OTA testing of 5G devices operating under mmWave massive MIMO channel conditions.

## REFERENCES

- [1] E. Bjornson, E. G. Larsson, and T. L. Marzetta, "Massive MIMO: Ten myths and one critical question," *IEEE Communication Magazine*, vol. 54, no. 2, pp. 114–123, 2016.
- [2] K. Sakaguchi, T. Haustein, S. Barbarossa, E. Strinati, A. Clemente, G. Destino, A. Pärssinen, I. Kim, H. Chung, J. Kim, W. Keusgen, R. Weiler, K. Takinami, E. Ceci, A. Sadri, L. Xain, A. Maltsev, G. K. Tran, H. Ogawa, and R. Heath, "Where, when, and how mmWave is used in 5G and beyond," *IEICE Transactions on Electronics*, vol. E100.C, 04 2017.
- [3] S. Sun, T. S. Rappaport, R. W. Heath, A. Nix, and S. Rangan, "MIMO for millimeter-wave wireless communications: Beamforming, spatial multiplexing, or both?" *IEEE Communications Magazine*, vol. 52, no. 12, pp. 110–121, 2014.
- [4] I. Hemadeh, S. Katla, M. El-Hajjar, and L. Hanzo, "Millimeter-wave communications: Physical channel models, design considerations, antenna constructions and link-budget," *IEEE Communications Surveys & Tutorials*, 12 2017.
- [5] M. Marcus and B. Pattan, "Millimeter wave propagation: spectrum management implications," *IEEE Microwave Magazine*, vol. 6, no. 2, pp. 54–62, 2005.
- [6] F. Qamar, M. Hindia, K. Dimiyati, K. Noordin, M. Bahjat, T. Abd Rahman, and I. Amiri, "Investigation of future 5G-IoT millimeter-wave network performance at 38 GHz for urban microcell outdoor environment," *Electronics*, vol. 8, 05 2019.
- [7] W. Fan, P. Kyosti, M. Rumney, X. Chen, and G. F. Pedersen, "Over-the-air radiated testing of millimeter-wave beam-steerable devices in a cost-effective measurement setup," *IEEE Communications Magazine*, vol. 56, no. 7, pp. 64–71, 2018.
- [8] P. Kildal, X. Chen, C. Orlienius, M. Franzen, and C. S. L. Patane, "Characterization of reverberation chambers for OTA measurements of wireless devices: Physical formulations of channel matrix and new uncertainty formula," *IEEE Transactions on Antennas and Propagation*, vol. 60, no. 8, pp. 3875–3891, 2012.
- [9] X. Chen, "Throughput modeling and measurement in an isotropic-scattering reverberation chamber," *IEEE Transactions on Antennas and Propagation*, vol. 62, no. 4, pp. 2130–2139, 2014.
- [10] E. Vlachos, G. C. Alexandropoulos, and J. Thompson, "Massive mimo channel estimation for millimeter wave systems via matrix completion," *IEEE Signal Processing Letters*, vol. 25, no. 11, pp. 1675–1679, 2018.
- [11] W. Yu, Y. Qi, K. Liu, Y. Xu, and J. Fan, "Radiated two-stage method for lte MIMO user equipment performance evaluation," *IEEE Transactions on Electromagnetic Compatibility*, vol. 56, no. 6, pp. 1691–1696, Dec 2014.
- [12] Y. Jing, H. Kong, and M. Rumney, "MIMO OTA test for a mobile station performance evaluation," *IEEE Instrumentation Measurement Magazine*, vol. 19, no. 3, pp. 43–50, 2016.
- [13] P. Kyosti, T. Jämsä, and J.-P. Nuutinen, "Channel modelling for multiprobe over-the-air MIMO testing," *International Journal of Antennas and Propagation*, vol. 2012, no. 615954, 2012.
- [14] W. Fan, X. Carreno, F. Sun, J. Nielsen, M. Knudsen, and G. Pedersen, "Emulating spatial characteristics of MIMO channels for OTA testing," *Antennas and Propagation, IEEE Transactions on*, vol. 61, pp. 4306–4314, 08 2013.
- [15] W. Fan, I. Carton, P. Kyösti, and G. F. Pedersen, "Emulating ray-tracing channels in multiprobe anechoic chamber setups for virtual drive testing," *IEEE Transactions on Antennas and Propagation*, vol. 64, no. 2, pp. 730–739, 2016.
- [16] A. Khatun, V. Kolmonen, V. Hovinen, D. Parveg, M. Berg, K. Haneda, K. I. Nikoskinen, and E. T. Salonen, "Experimental verification of a plane-wave field synthesis technique for MIMO OTA antenna testing," *IEEE Transactions on Antennas and Propagation*, vol. 64, no. 7, pp. 3141–3150, 2016.

- [17] Y. Miao, W. Fan, J. Takada, R. He, X. Yin, M. Yang, J. Rodríguez-Piñeiro, A. A. Glazunov, W. Wang, and Y. Gong, "Comparing channel emulation algorithms by using plane waves and spherical vector waves in multiprobe anechoic chamber setups," *IEEE Transactions on Antennas and Propagation*, vol. 67, no. 6, pp. 4091–4103, 2019.
- [18] P. Kyösti, L. Hentilä, W. Fan, J. Lehtomäki, and M. Latva-Aho, "On radiated performance evaluation of massive MIMO devices in multiprobe anechoic chamber OTA setups," *IEEE Transactions on Antennas and Propagation*, vol. 66, no. 10, pp. 5485–5497, Oct 2018.
- [19] "Study on channel model for frequencies from 0.5 to 100 GHz," Tech. Rep., 3GPP TR 38.901 V16.1.0, Jan 2020.
- [20] X. Cai, G. Zhang, C. Zhang, W. Fan, J. Li, and G. F. Pedersen, "Dynamic channel modeling for indoor millimeter-wave propagation channels based on measurements," *IEEE Transactions on Communications*, vol. 68, no. 9, pp. 5878–5891, 2020.
- [21] X. Cai and W. Fan, "A complexity-efficient high resolution propagation parameter estimation algorithm for ultra-wideband large-scale uniform circular array," *IEEE Transactions on Communications*, vol. 67, no. 8, pp. 5862–5874, Aug 2019.
- [22] M. Rumney, P. Kyösti, and L. Hentilä, "3GPP channel model developments for 5G NR requirements and testing," in *12th European Conference on Antennas and Propagation (EuCAP 2018)*, 2018, pp. 1–5.
- [23] P. Kyösti, L. Hentilä, J. Kyröläinen, F. Zhang, W. Fan, and M. Latva-aho, "Emulating dynamic radio channels for radiated testing of massive MIMO devices," in *12th European Conference on Antennas and Propagation (EuCAP 2018)*, 2018, pp. 1–5.
- [24] 3GPP document, R4-1904116, "Study of channel model impact on FR2 MPAC test solution," Spirent Communications, April, 2019.
- [25] 3GPP document, R4-2002073, "System design and probe layout for FR2 MPAC MIMO OTA," Spirent Communications, Feb, 2020.
- [26] A. Alkhateeb and R. W. Heath, "Frequency selective hybrid precoding for limited feedback millimeter wave systems," *IEEE Transactions on Communications*, vol. 64, no. 5, pp. 1801–1818, May 2016.
- [27] S. A. Busari, K. M. S. Huq, S. Mumtaz, L. Dai, and J. Rodriguez, "Millimeter-wave massive MIMO communication for future wireless systems: A survey," *IEEE Communications Surveys Tutorials*, vol. 20, no. 2, pp. 836–869, Secondquarter 2018.
- [28] A. Alkhateeb, J. Mo, N. Gonzalez-Prelcic, and R. W. Heath, "MIMO precoding and combining solutions for millimeter-wave systems," *IEEE Communications Magazine*, vol. 52, no. 12, pp. 122–131, December 2014.
- [29] "Study on new radio access technology-Physical layer aspects," Tech. Rep., 3GPP TR 38.802 V14.2.0, Sep. 2017.
- [30] X. Yin, S. Wang, N. Zhang, and B. Ai, "Scatterer localization using large-scale antenna arrays based on a spherical wave-front parametric model," *IEEE Transactions on Wireless Communications*, vol. 16, no. 10, pp. 6543–6556, Oct 2017.
- [31] X. Cai, W. Fan, X. Yin, and G. F. Pedersen, "Trajectory-aided maximum-likelihood algorithm for channel parameter estimation in ultrawideband large-scale arrays," *IEEE Transactions on Antennas and Propagation*, vol. 68, no. 10, pp. 7131–7143, 2020.
- [32] *METIS Channel Models, Deliverable D1.4 v1.3*, document ICT-317669 METIS Project, 2015.
- [33] P. Kyösti, J. Nuutinen, J. Kolu, and M. Falck, "Channel modelling for radiated testing of MIMO capable terminals," in *ICT Mobile Summit Conference*, June 2009, pp. 1–8.
- [34] M. Giordani, M. Polese, A. Roy, D. Castor, and M. Zorzi, "A tutorial on beam management for 3GPP NR at mmwave frequencies," *IEEE Communications Surveys and Tutorials*, 2019.
- [35] P. Kyösti, W. Fan, G. F. Pedersen, and M. Latva-Aho, "On dimensions of OTA setups for massive MIMO base stations radiated testing," *IEEE Access*, vol. 4, pp. 5971–5981, 2016.
- [36] A. W. Mbugua, W. Fan, K. Olesen, X. Cai, and G. F. Pedersen, "Phase-compensated optical fiber-based ultrawideband channel sounder," *IEEE Transactions on Microwave Theory and Techniques*, vol. 68, no. 2, pp. 636–647, 2020.